Chapter 10

Guiding On-Chip Optical Beams Without Diffraction in a Rod-Type Silicon Photonic Crystal

Wei Li, Hao Li, Ming Li, Haiyang Huang and Fuwan Gan

Additional information is available at the end of the chapter

http://dx.doi.org/10.5772/67949

Abstract

Guiding on-chip optical beams without diffraction is very important in the future's all-photonic circuits. Herein, both theoretically and experimentally, we study an all-angle quasi-self-collimation phenomenon occurring in photonic crystals composed of silicon nanorods. When the all-angle quasi-self-collimation phenomenon occurs, the optical beams can be incident onto such photonic crystals from directions covering a wide range (extremely close to all-angle) of incident angles direction and become highly localized along even a single array of rods, which finally achieve results in the narrow-beam propagation without divergence. The propagation length is expected to be 1000 times larger than the wavelength of light. Theoretically, it is shown that such all-angle quasi-self-collimation phenomenon is owing to the symmetry change of the lattice of photonic crystals. By changing the symmetry of a photonic crystal to straighten the isofrequency contours, the photonic crystal shows the all-angle quasi-self-collimation effect. Experimentally, we show the observation of all-angle quasi-self-collimation phenomenon occurring in a rod-type silicon photonic crystal fabricated on by patterning a silicon-on-insulator (SOI) wafer. The experimentally observed propagation length is more than 0.4 mm over the telecom wavelength range, even though at large angle of incidence, which is a relatively large length scale for on-chip optical interconnection.

Keywords: without diffraction, silicon photonic crystal, all-angle quasi-self-collimation, SOI

INTECH
open science | open minds

© 2017 The Author(s). Licensee InTech. This chapter is distributed under the terms of the Creative Commons Attribution License (http://creativecommons.org/licenses/by/3.0), which permits unrestricted use, distribution, and reproduction in any medium, provided the original work is properly cited. CC BY

1. Introduction

By using an index gradient, a well-designed waveguide array [1], or nonlinear optical effects [2, 3], beam spreading arising from geometrical origin can be manipulated in many ways. Photonic crystals (PCs) provide an alternative to beam steering based on photonic band-gap (PBG) formation and related dispersion phenomena such as negative refraction, super-prisms, and slow light. Self-collimation (SC) as a dispersion-related phenomenon is worth studying because it has important implications for subwavelength focusing, channel-less waveguiding and diffraction suppression [4–7], etc. In a SC PC, the light beams can propagate without diffraction, since propagation directions are paralleled to the group velocity, i.e., $V_g = \nabla_k \omega(k)$, where ω is the optical frequency for a determined wave vector k. Thus, we can determine that the SC effect is ascribed to the flat part of the equifrequency contours (EFCs) [8, 9]. Based on the SC effect, it can be used to design novel SC-based photonic devices, such as devices for diffraction inhibition, channel-less waveguides, subwavelength focusing or imaging [4, 5, 10, 11].

In recent years, the development of fabrication techniques has enabled the SC PCs to function at optical frequencies. In experiments, it has been recognized that SC phenomenon exists in many different kinds of structures, containing pillar-type and hole-type PCs [4, 12, 13], and quasi-zero-average-index structures [14], or even three-dimensional PCs [15]. Lately, wide-angle SC phenomena have been reported in PCs with square lattices by the composition of elliptical air holes [16]. Technically speaking, contrary to the hole-type PC, there are a great potential for active components with the pillar-type structure, benefiting from the possibility of the heat dissipation capability and electrical contraction. In addition, the light interacts with the medium (to be sensed) which more strongly surrounds the rods, and in optofluidics, the rod structure allows for fluid penetration better than the structure composed of air holes in a dielectric slab, therefore, the rods are more suitable for sensing applications.

However, there are still some problems to be solved. For example, the SC effect may be limited by the angle of incidence of light, which makes SC-based super-integrated devices difficult to manufacture. In this paper, the model is clarified for a full-angle quasi-SC PC, and the lower reflections for our quasi-SC PC by utilizing the destructive interference-based method. This all-angle quasi-SC is related to a flat equifrequency contour (EFC) across the entire Brillouin zone. In contrast to the conventional self-collimation, the all-angle quasi-SC shown in this chapter exhibits two unique properties. First, the light waves can be injected from any angle, even up to 90° [17]. Second, the electromagnetic energy can be achieved for high degree of localization in the case of nondiffraction [5]. For hole-type PCs, light waves are confined between the pores owing to the full-angle quasi-SC phenomenon, whereas for pillar-type PC, the electromagnetic energy can be positioned highly along a narrow path just as in a single nanorod array, as presented in this paper. Moreover, we will also show our recent experimental work on the all-angle quasi-SC in PCs composed of silicon nanorods. We believe this work motivates the current research on silicon photonics.

http://dx.doi.org/10.5772/67949

2. Theoretical model and analysis

First, the two-dimensional (2D) rod-shaped silicon PC is considered with a rectangular lattice in the air, as shown on the inset in **Figure 1(a)**. The breadth and length of the rectangular lattice are denoted by a and b, respectively, and the radius of the rod is $r = 0.3a$. Assume that the silicon rod is lossless and nondispersive near the telecommunication frequency and exhibit a refractive index of 3.5. Then, EFCs can be calculated by plane-wave expansion method. To simplify the model throughout this chapter, only one single frequency $f = 0.2\ c/a$ is considered for the transverse electric (TE) modes. This frequency is located in the first photonic band, and the corresponding isofrequency contour plot is shown in **Figure 1**.

2.1. Straightness of the EFCs and collimation ability of the beams

As shown in **Figure 1(a)–(d)**, the large angle SC effect in PC can be obtained by changing the symmetry of the PC, that is, by increasing the aspect ratio of the length to breadth "β = b/a". As shown in **Figure 1(d)**, the large angle SC effect is indicated by the straightness of the EFC

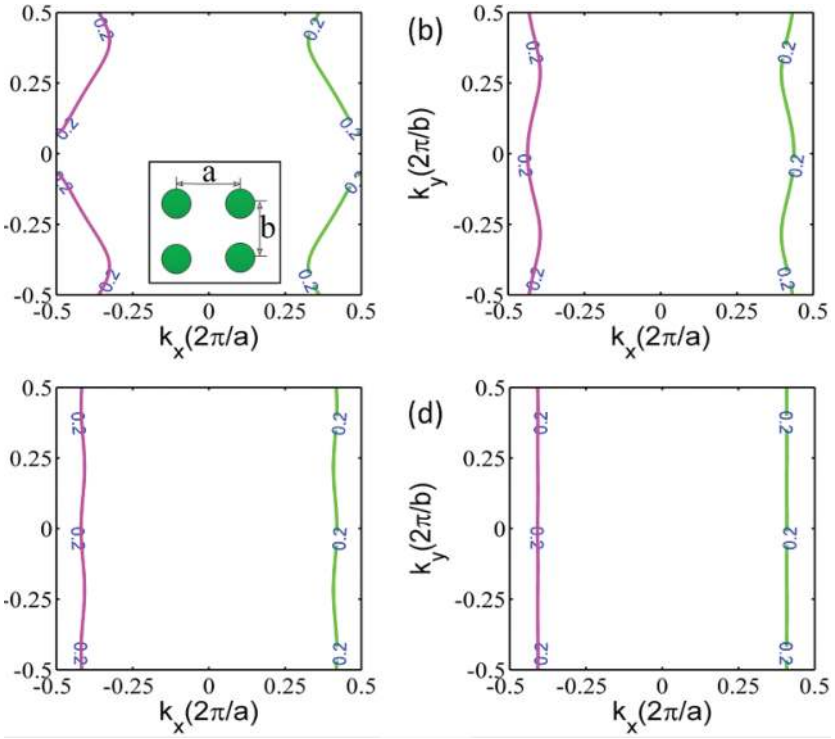

Figure 1. EFCs for the normalized frequency $f = 0.2c/a$, fixed a, $r=0.3a$, and different lattice length-breadth ratios β: (a) β = 1.25, (b) β = 1.75, (c) β = 2.3, and (d) β = 3.5. Inset image in (a): schematic illustration of the 2D PC.

plotted over the entire Brillouin zone. The light beams can reduce beam divergence along with the increase of β value, resulting in self-collimation propagation along the *ΓX* direction. Therefore, for the purpose of improving the collimation ability, a higher EFC straightness must be obtained. As described in **Figure 1**, the straightness linearity of the EFCs is determined by β.

In order to study the correlation between length-breadth ratio "β" and EFC straightness, the least-squares method [17] is used to quantify EFC straightness as shown in **Figure 1**. According to this method, a quasistraight EFC whose curve can be illustrated by a function "Y = F(X)" (Y representing ky and X representing kx). Assuming that a straight line with the equation

$$\overline{Y} = AX + B \tag{1}$$

can be applied to fit the quasistraight EFC, where A and B are undetermined coefficients. For the purpose of obtaining A and B, $\varepsilon = \sum_{i=1}^{n} \left[Y_i - \left(A X_i + B \right) \right]^2$ is defined, where *i* is the number of sampling points, then, by utilizing the minimum condition, i.e., ∂ε/∂A, ∂ε/∂B, we obtain

$$A\sum X_i^2 + B\sum X_i = \sum X_i Y_i \tag{2}$$

and

$$A\sum X_i + nB = \sum Y_i \tag{3}$$

From Eqs. (2) and (3), A and B can be calculated as follows:

$$A = \frac{n\sum X_i Y_i - \sum X_i \sum Y_i}{n\sum X_i^2 - \left(\sum X_i\right)^2} B = \frac{\sum Y_i \sum X_i^2 - \sum X_i \sum X_i Y_i}{n\sum X_i^2 - \left(\sum X_i\right)^2} \tag{4}$$

Finally, we can quantify the straightness quality of the EFCs through the straightness factor

$$L = \Delta L_{max} - \Delta L_{min} \tag{5}$$

Where $\Delta L_{max} = [Y - \overline{Y}]_{max} = [Y - AX - B]_{max}$ and $\Delta L_{min} = [Y - \overline{Y}]_{min} = [Y - AX - B]_{min}$ are the maximum and the minimum convexities, respectively.

According to the straightness factor L is defined by Eq. (5), the averaged deviation angle of the propagation direction can be illustrated for a quasi-collimated light beam. Furthermore, we note that the beam width will become broader while the beam propagates through the quasi-SC PC, with determining the beam waist by $W(D) \approx W_0 + L\frac{\lambda D}{\pi W_0}$ where λ is the wavelength in the air, W_0 and D (we assume $D \gg \lambda$, $D \gg W_0$) describe the initial waist and propagation distance of the beam, respectively. The smaller L corresponds to a straighter EFC and better self-collimation behavior. Just in case L = 0, a perfectly straight EFC corresponding to a strict self-collimation without beam divergence is obtained, $W(D) = W_0$ which the D can take any value.

For most practical applications, the condition L = 0 is too strict. A sufficiently small L is usually acceptable. We proposed $L_0 = 0.01$ as the critical value for the straightness factor (corresponding to the pink dash line in **Figure 2**). In this case, the quasi-collimated beam shows almost no diffraction if $L \le L_0$, for example, relative to a typical Gaussian beam with an initial waist $W_0 = 10\lambda$, the

http://dx.doi.org/10.5772/67949

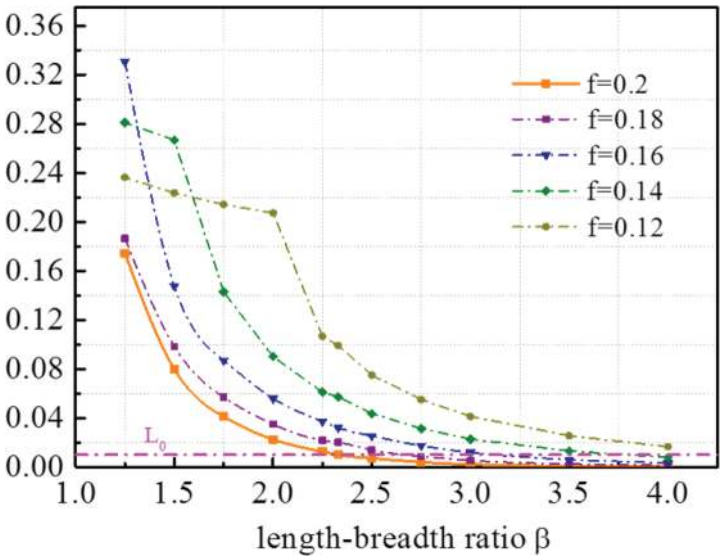

Figure 2. Straightness factor L plotted as a function of the length–breadth ratio β of the rectangular lattice. The normalized frequencies are in unit of c/a.

beam broadening is less than 1% as the beam propagates at a distance scale of 100λ. We consider this quasi-collimated beam to be sufficient for most practical applications with self-collimation phenomenon.

Using Eq. (5), the straightness factor L of the EFCs can be calculated. **Figure 2** shows the relationship between the straightness factor of the EFCs and the rectangular lattice structure. As β increases, the straightness factor L decreases obviously. This result is consistent with the result in **Figure 1**. As shown in **Figure 1(a)–(d)**, we can measure that the corresponding straightness factors are $L = 0.1743$, $L = 0.014$, $L = 0.01$, and $L = 8.09 \times 10^{-4}$, respectively. For $f = 0.2c/a$, which is the normalized frequency, the condition $L = L_0$ corresponds to $\beta = 2.3$, with the corresponding EFC shown in **Figure 1(c)**. In order to provide usable operating frequency quasi-SC effect on additional information, L in the other four frequencies as a function of β is also shown in **Figure 2**, from which they can be seen with $f = 0.2c/a$ very similar. Furthermore, bandwidth of quasi-SC effect becomes broader and broader by increasing β, because more and more EFCs have their straightness factor L smaller than L_0.

As shown in **Figure 2**, it is possible to realize a better and better SC by increasing β. For the case of $\beta \gg 1$, the system will become separated from each other, so in this case, we can investigate only one of the row of rods. We find that the SC effect is still valid in this single row of rods. However, there are many differences between their single row, and also there are many differences between a single row and a PC having a rectangular lattice. For the sake of simplicity, we limit ourselves to only explore the PC shown in **Figure 1**(with $\beta = 2.3$) at a single frequency $f = 0.2c/a$.

In order to study the whole-angle quasi-collimation phenomenon of the PC at the frequency $f = 0.2c/a$, with $\beta = 2.3$, $a = 0.4$ μm, and $r = 0.3a$, a Gaussian beam with the beam width 2.3 μm (a little bit larger than one wavelength 2 μm) is incident to the PC at any incident angle. **Figure 3** shows the calculation model, which can be applied to calculate the electromagnetic field by a perfectly matched layer (PML) finite-difference-time-domain (FDTD) method [10, 11] with a grid size 20 nm. The PC's right, 50 × 71 rods array (as shown in the blue bars in **Figure 3**) are manually set to be absorbed (a small imaginary part is added to the refractive index of rod, i.e., the index becomes 3.5 + 0.02i) which set to avoid the size-dependent Fabry-Perot effect. A PML boundary condition is acted by absorption rods array for the PC. Thus, the structure may be available to simulate an infinite-length PC. As shown in **Figure 4** and the subsequent figures, the field distribution is presented. However, only the field which is located in the nonabsorption region is shown. When a Gaussian beam propagates with a different incident angle in air (top panels) and PC (lower panels), the field distribution in this case is depicted in **Figure 4(a)–(c)**. We can see that the beam does not diverge in the PC which shown in **Figure 4**. On the contrary, the electron beam has great divergence in the air.

2.2. Coupling analysis

We investigate the optical coupling efficiency of the SC PC in this section. Owing to strong reflection, there are the large coupling losses (about 50%), which are shown in **Figure 4**. For improving the coupling efficiency, we propose a method based on destructive interference. **Figure 5** depicts an antireflection layer (ARL), which is used in front of the quasi SC PC. The ARL is also constituted of the silicon rods array, which a lattice constant $b = 2.3a$ is equal to the length of the rectangular lattice of the quasi-SC PC. The silicon rods radius in the ARL is

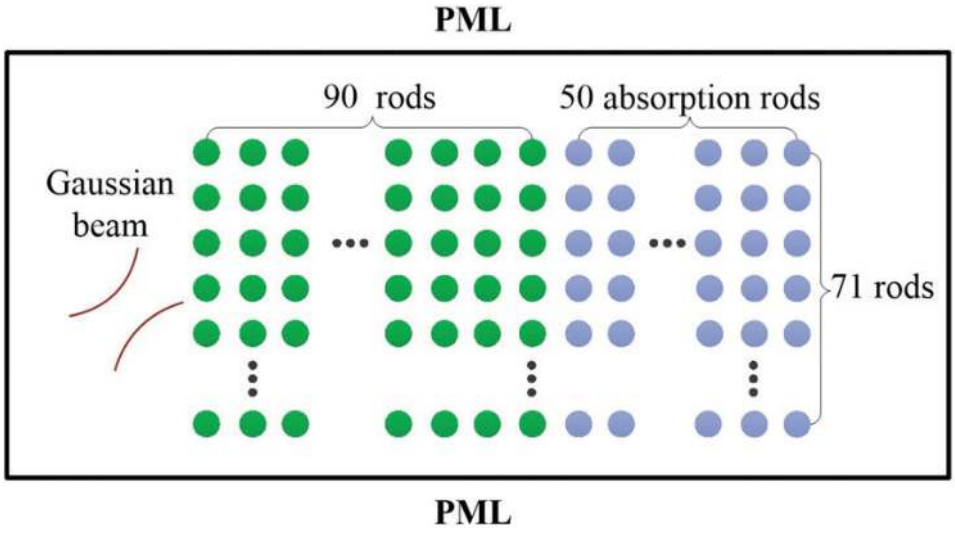

Figure 3. FDTD calculation model.

http://dx.doi.org/10.5772/67949

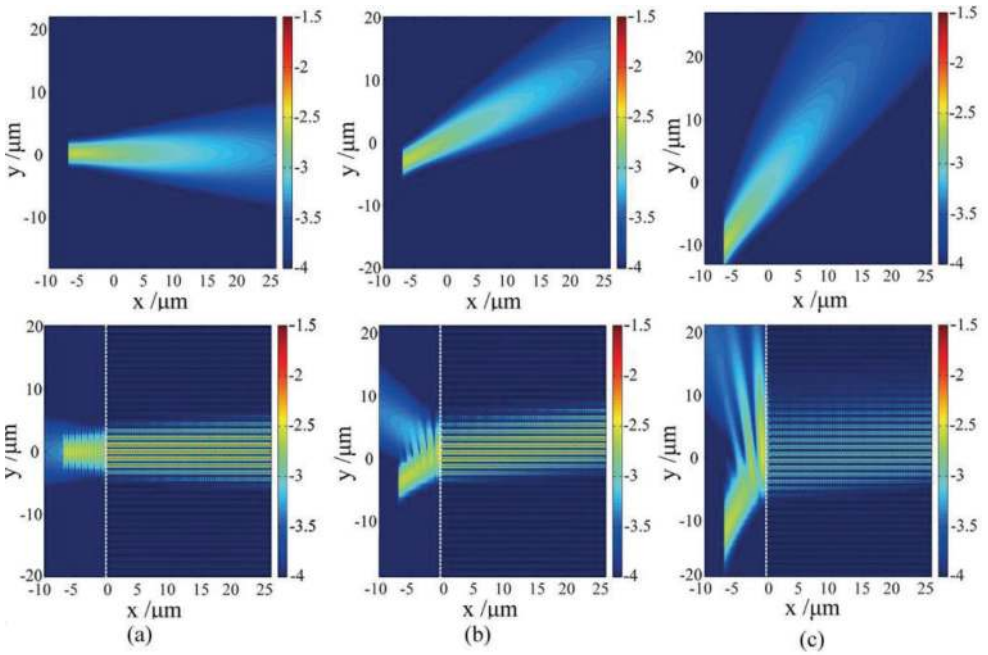

Figure 4. The field distribution when Gaussian beam irradiated to the air (top panel) and PC (lower panel) having different incident angles θ: (a) θ = 0°, (b) θ = 30°, and (c) θ = 30°. The white dashed line presents the interface between the air and PC, and the field distribution is plotted using a logarithmic color map .

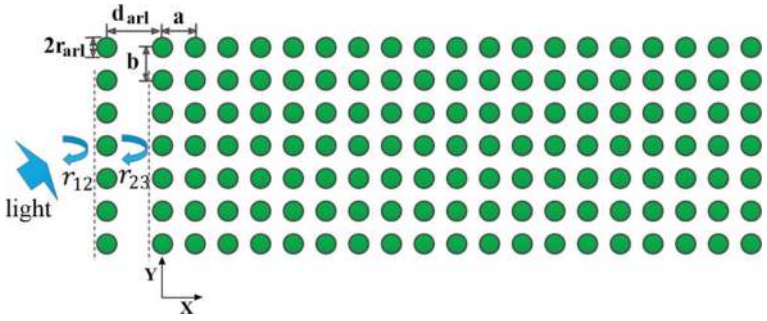

Figure 5. Schematic illustration of the ARL placed in front of the quasi-SC PC. The variable ARL parameters are the distance d_{arl} and the radius r_{arl} .

r_{arl}, and the distance between the ARL and the quasi-SC PC is d_{arl}. The parameters d_{arl} and r_{arl} should be well-designed to improve the coupling efficiency.

The coupling efficiency $\kappa = 1 - \left| r_{tot} \right|^2$ is directly determined by the total reflection coefficient r_{tot}, which can be written as:

$$r_{tot} = \frac{r_{12} + r_{23} e^{i2\beta}}{1 + r_{12} r_{23} e^{i2\beta}} \tag{6}$$

where $\beta = k_0 \cdot (d_{arl} - r - r_{arl})$ is the phase shift of the light beam as it crosses the ARL (k_0 denotes the wave vector in the air), r_{12} is the reflection coefficient of the ARL and r_{23} is the reflection coefficient of the semi-infinite quasi-SC PC in the air when the light beam is striking the PC surface from air. By applying the multiple scattering method [18], both r_{12} and r_{23} can be calculated.

We try to find the appropriate r_{arl} and d_{arl} values to reduce total reflection $|r_{tot}|^2$. First, we calculate the coupling efficiency for an initial value of r_{arl} with $r_{arl} = r$, and the resulting color map is shown in **Figure 6(a)**. In this figure, the red area corresponds to high coupling efficiency. As shown in **Figure 5**, there are two regions, which allow for high coupling efficiency over a relatively wide incidence angle. We can select the appropriate d_{arl} according to **Figure 1**. As shown in **Figure 5**, for instance, 3.28a for an incident angle of 0°–20°, or 3.44a for an incident angle of 20°–30°. Then, for the optimization of d_{arl}, r_{arl} can be further optimized by improving the coupling efficiency, as shown in **Figure 6(b)** and **(c)**. The d_{arl} values are fixed to be 3.28a and 3.44a, respectively. From **Figure 6(d)**, the enhanced coupling efficiency is described versus the

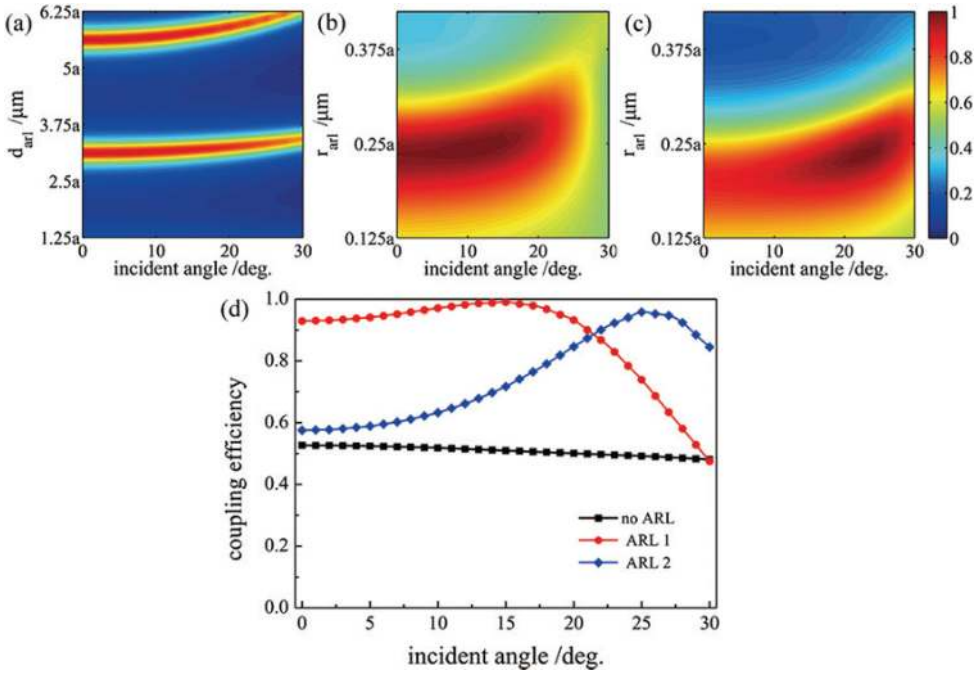

Figure 6. (a) The coupling efficiency as a function of d_{arl} and the incident angle, which d_{arl} and r_{arl} are fixed at 0.3a. (b) The coupling efficiency as a function of r_{arl} and the incident angle θ, which an optimized d_{arl} is fixed at *3.28a*. (c) The coupling efficiency as a function of r_{arl} and an incident angle θ which an optimized d_{arl} is fixed at *3.44a*. (d) Coupling efficiency as a function of the incident angle without and with ARL. The structure parameters of ARL 1 and ARL 2 are $d_{arl} = 3.28a$, $r_{arl} = 0.26a$ and $d_{arl} = 3.44a$, $r_{arl} = 0.26a$, respectively.

http://dx.doi.org/10.5772/67949

incident angle. The coupling efficiency is greatly improved over a wide incidence angle range by using the well-designed ARL.

In order to further improve the coupling efficiency, graded multiple ARLs are provided with same lattice constant (b = 2.3a) as shown in **Figure 7(a)**. They locate in front of the photonic crystal, which the distance is a. There are 20 layers in the graded multiple ARLs, and the rods radius is varying from the left to the right slowly, i.e., for the ith layer, the radius of the rods is $r_{ARLs}(i) = i(r/20)$, where i = 1, 2,…, 20. By using the multiple ARLs, the coupling efficiency is improved for nearly all incident angles, as shown in **Figure 7(b)**.

In order to verify the improvement of the coupling efficiency, the field distribution is calculated for the Gaussian beam at four angles of incidence emitted at a PC with multiple ARLs, and the resulting field distribution is described in **Figure 8(a)–(d)**, respectively. For multiple ARLs structure, the Gaussian beams are almost completely coupled into the PC with little reflection. Comparing **Figure 8** with **Figure 4**, it is indicated that the multiple ARLs can suppress the reflection.

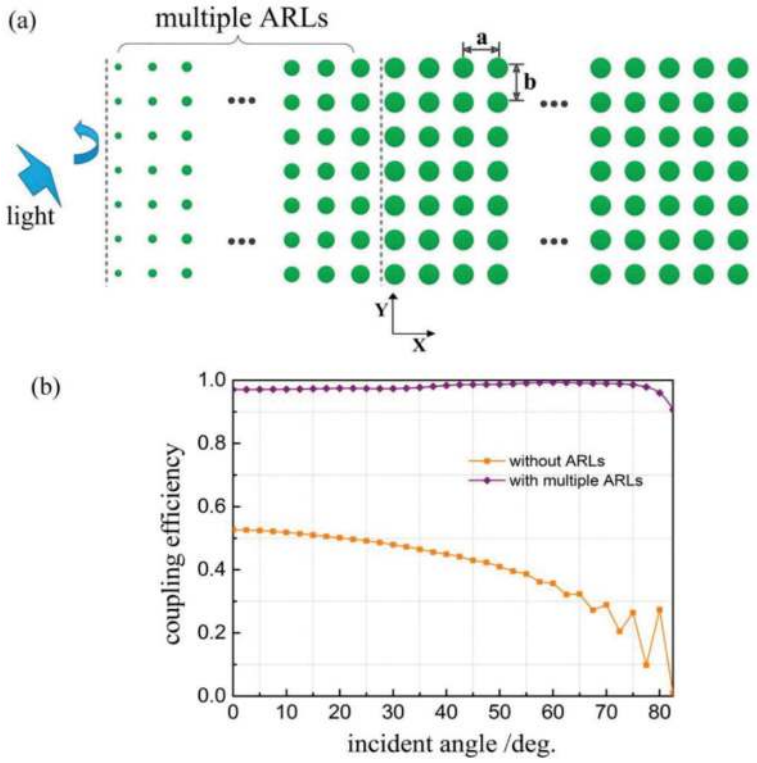

Figure 7. (a) Schematic illustration of the multiple ARLs. (b) Coupling efficiency as a function of the incident angle without and with multiple ARLs.

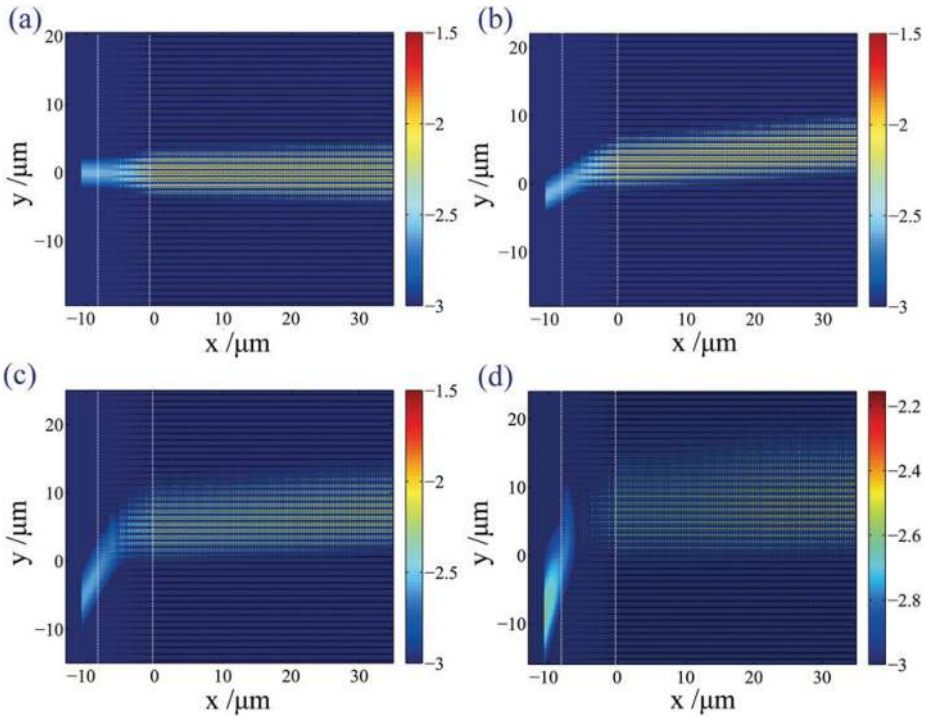

Figure 8. Field distribution when Gaussian beam emitting at the PC with multiple ARLs at different incident angles θ: (a) θ = 0°, (b) θ = 30°, (c) θ = 60°, and (d) θ = 75°. The white dashed line presents the interface, and the field distribution is described using a logarithmic color map.

3. Experimental model, results and discussion

We present the demonstration of a full-angle quasi-SC phenomenon based on pillar-type PCs in this section. Light waves are received into these pillar-type PCs from a wide range of incidence angles and can be positioned highly along the array of rods. We observed that the propagation length was 0.4 mm in the wavelength range of 1540–1570 nm. For on-chip photonic applications, this value might be sufficient propagation distance.

3.1. Experimental model

In order to increase the angular collimation range, a simple and feasible approach is to reduce the symmetry of the photonic construct by using a rectangular lattice [19]. Here, the 2D pillar-type PC composed of a rectangular lattice fabricated by patterning silicon on insulator (SOI) wafer, as presented in **Figure 9(a)**. By increasing a rectangular lattice of side ratio, a flat EFC across the entire Brillouin zone can be obtained. However, due to the small filling factor of the dielectric material, an excess ratio will result in leakage of the light wave in the other direction

http://dx.doi.org/10.5772/67949

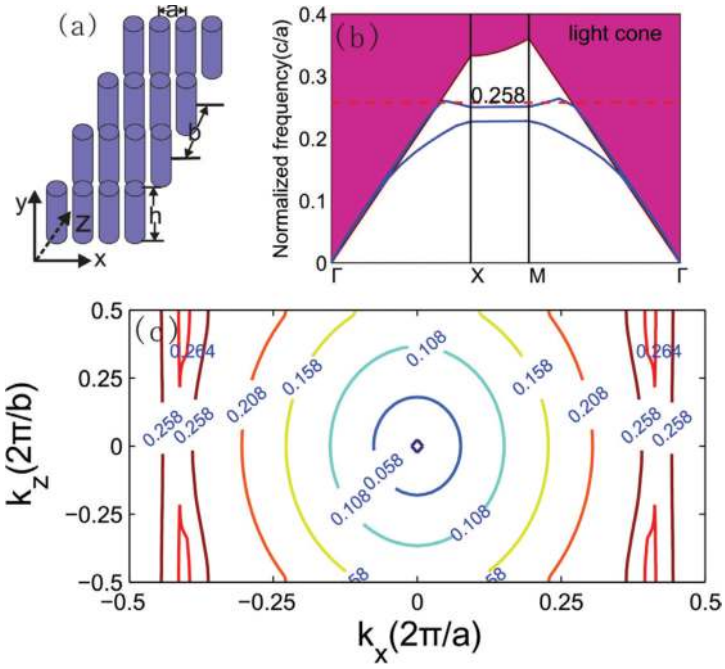

Figure 9. (a) Schematic diagram of a 2D pillar-type PC, which consists of a rectangular lattice formed by patterning the SOI wafer. (b) Band diagram of rectangular lattice PC. The dashed line indicates the frequency as 0.258c/a. The colored area describes a light cone. (c) An equifrequency contours of the second frequency band.

(z-direction). As a compromise between the full-angle quasi-self-collimation effect and the collimating efficiency, we choose a PC structure with $b/a = 2.4$. A top silicon layer with a height $h = 2{:}025a$ was used as a board layer. The buried oxide (BOX) layer forms a high refractive index-contrast structure with the air as the cladding. According to this particular structure, out-of-plane light confinement is achieved owing to total internal reflection. For the silicon and BOX, the refractive indices are $n_{Si} = 3.5$ and $n_{SiO2} = 1.5$, respectively. Using plane wave expansion (PWE), we can obtain the band diagrams for the TM-like polarization (with the E-field along the *y*-direction), as shown in **Figure 9(b)**. The colored area is a light cone, below which are guided mode to be positioned in the plate [20, 21].

The light propagation direction in PCs depends entirely on the gradient direction of the corresponding EFC, since the propagation direction is the same as the group velocity $v_g = \nabla k\omega$ (k), where ω is the optical frequency corresponding the wave vector k [22]. Thus, we can consider that the self-collimation effect is derived from the flat portion of the EFC. However, the non-diffractive propagation is confined owing to the use of a relatively broad beam of light, which the wave vectors are limited to the local flat portion of the EFC. For a narrow beam including a large range of k vectors, for instance, to obtain all-angle quasi-self-collimation, we require a flat EFC across the entire first Brillouin zone (as we discussed in the above section). Then, we calculate the corresponding EFC of the second frequency band as shown in **Figure 9(c)**.

It is noteworthy that, at the f = 0.258 c/a, the flat EFC is flat across the first Brillouin zone, which is expected to lead to a large angle self-collimation. To validate our prediction, 3D finite difference time domain (FDTD) method is used to perform the simulation. A Gaussian beam having a width of 0.25b at f = 0.258 c/a is emitted into the designed PC. The calculated electric field intensity is drawn in **Figure 10(a)**. The self-calibration is achieved even though the small beam circumference, which the light source contains a wide range of k vectors. The E_y field intensity is presented along the z-direction at x = 40a in **Figure 10(b)**. It is noteworthy that the EM energy is highly positioned along the array of a single nanorod. The E_y field intensity is only $1/10^5$ which located in the third row to each one side of this single nanorod array, for instance, a very weak electric field. It will ensure good confinement for light waves when placing of four rows of nanorods on each side of the central single nanorod array.

3.2. Experimental results and discussion

The parameters of the dielectric nanorod chain design is a = 400 nm, r = 160 nm, and h = 810 nm for which these operate at frequencies of optical communications. The PC is fabricated on a platform of silicon-on-insulator (SOI) wafers by four main processing steps. First, we require that thermal oxidation is needed to form an oxide layer, which serves as a hard mask for the purpose of transferring the pattern into the Si layer by using reactive ion etching (RIE). Second, we apply electron beam (E-beam) lithography to transfer this pattern to the high-sensitivity and high-resolution E-beam Resist ZEP-520. Third, the hard mask is etched using RIE in a CHF_3 plasma. Finally, after using the inductively coupled plasma (ICP) etching process, which a thermally grown SiO_2 layer is used as a hard mask, the resulting dielectric rods are about 810 nm. **Figure 11** shows the scanning electron microscope (SEM) image of the nanorods, the rods have sidewall profiles approximately 90° to the substrate; the screw thread is caused by deep etching with using the Bosch process.

To show the large angle of self-collimation effect, three different samples with tilted PC areas were designed in the experiment. We introduce light waves to irradiate the PCs by a waveguide, which a width is 3 m as shown in left panels (a), (b), and (c) of **Figure 12**, it is designed that the tilt angles with respect to the incident waveguide are set to be 0°, 45°, and 75°, respectively. Theoretically, note that self-collimation can even be observed for an incident angle of almost 90°. However, due to impedance mismatch, larger incident angle causes more

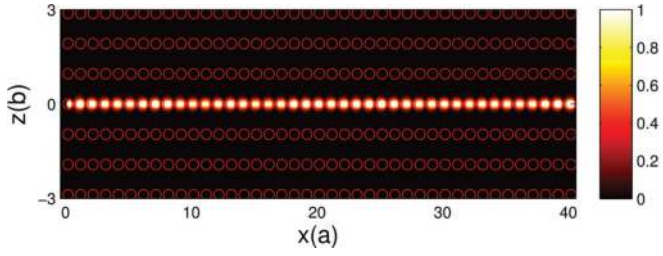

Figure 10. (a) The field intensity of the electric field component *Ey* (TM polarization) calculated using the FDTD method. (b) The *Ey* field intensity along the z-direction at x = 40a.

http://dx.doi.org/10.5772/67949

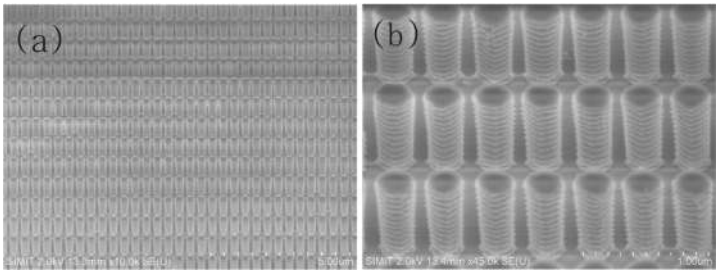

Figure 11. SEM images of the fabricated device: (a) Rectangle lattice pillar-type PCs with a = 400 nm, b = 2.4a, and h = 2.025a. (b) Magnified image.

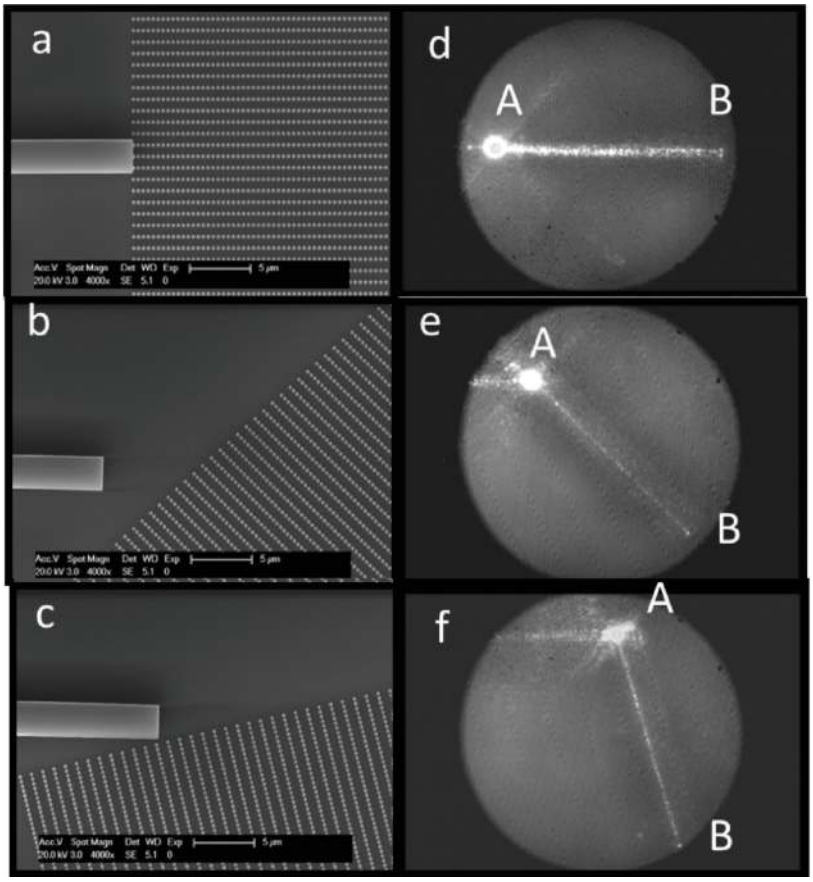

Figure 12. The left part of FIG: SEM images of PC samples with different tilt angle (a) 0°, (b) 45°, and (c) 75°. The right part of FIG: (d), (e), and (f): a top view of the scattered light, which indicates the ray trace of the light beam captured by the infrared camera. A and B are marks of the light spots generated by strong scattering at the interface.

reflection losses. In our experiments, the maximum incident angle is set at 75°, so that our camera can be used to capture a sufficient amount of light scattering due to structural defects. The TM polarized light from the tunable laser source is introduced into the lensed fiber. In order to visualize the EM energy transfer in the PC, we use an infrared camera to capture the ray trajectory of the EM energy (through the scattered light). Light traces were observed clearly in the 1540–1570 nm wavelength range. Coupled resonator waveguides (CROWs) based on weak coupling between high-Q cavities can also achieve functions similar to those of our guided-wave PC structures. Unfortunately, their operating frequencies are limited to the resonant frequencies of the whispering gallery modes of individual rods [23]. In contrast, our SC effect is based on the dispersion relation of the entire PC, operating over a bandwidth wider than the resonant frequency of a single rod. **Figure 12(d)–(f)** corresponds to capturing the results at 1550 nm wavelength with incident angles of 0°, 45°, and 75°, respectively. At the point of A, this light spot is contributed by strong scattering which located on the interface of the waveguide surface and the PCs. At the point of B, this light spot which situated at the opposite end of the PC region, also provides an interface for optical scattering. There are 1000 lattice periods in the routing from A and B, corresponding to the propagation length value of 0.4 mm. For the on-chip optical interconnection, it is a very considerable length scale. For the large-angle self-collimation effect, previous experiments shown that the light propagating had at least 100 lattice periods without significant divergence [24]. In our experiment, the propagation length can be as high as 1000 lattice periods, and ray trajectory of the light is clearer than the previous.

For a detailed description of the quantitative results, the field intensity of the nanorod array determined from the FDTD calculations [25] is plotted in **Figure 13(a)**. The experimentally determined propagation loss of the self-collimated beam is measured by plotting the relative intensity along the nanorods in **Figure 12(d)**. The experimental propagation loss is determined to be 17.6 dB/mm, which is higher than the simulation result as shown in **Figure 13**. It is believed that the extra propagation loss is mainly attributed to the

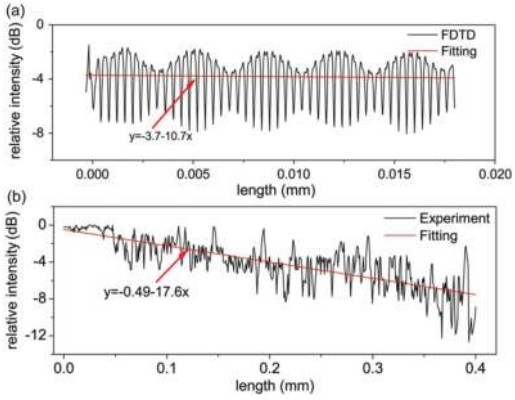

Figure 13. (a) Theoretical propagation loss from the 3D FDTD simulation. (b) Experimental propagation loss of the self-collimated beam determined by plotting the relative intensity (in logarithmic scale) along the nanorods in **Figure 11(d)**.

http://dx.doi.org/10.5772/67949

roughness of the pillars, but we can reduce this roughness by improving the manufacturing process. Our simulation shows that the coupling efficiency can be as high as 92, 90, and 45% corresponding to the incident angles of 0°, 45°, and 75°, respectively. Furthermore, through modifying the interface [26, 27], the coupling efficiency can be enhanced by suppressing scattering at the point A. Therefore, it is believed that the millimeter-scale propagation length can be easily observed with the rod structure based on the above-mentioned improvements.

4. Conclusion

In conclusion, an all-angle quasi-self-collimation effect can be achieved by changing the rectangular-lattice symmetry of photonic crystal. The quasi-self-collimation effect is identified and quantified by a straightness factor L, which is based on the least-squares method. With the decrease of straightness factor L, the photonic crystal possesses a more powerful self-collimation effect. Besides, the efficiency of light coupling to the quasi-self-collimation photonic crystal is investigated and is greatly improved by applying a carefully designed antireflection structure. Experimentally, we have designed, fabricated, and characterized a structure based on silicon nanorods that exhibits the all-angle quasi-SC phenomenon. The millimeter-scale propagation length and broad wavelength range exhibited by our structure may be sufficient for on-chip photonic applications. Our recent study shows such all-angle quasi-self-collimation effect can also be used to design a compact silicon nanoantenna array for high-efficiency vertical light emission [28]. Such a large-angle SC phenomenon resulting from the nanorod structure may also find applications in sensing and optofluidics.

Acknowledgments

This research was sponsored by the National Natural Science Foundation of China (Grant Nos. 61475180, and 61275112), and the Science and Technology Commission of Shanghai Municipality (Grant Nos. 14JC1407601, and 14JC1407602). The figures in this chapter were extracted from our previous papers (H. Li et al, IEEE Photon. J. 5, 2201306 (2013) and M. Li et al., IEEE Photon. J. 7, 4700108 (2015)).

Author details

Wei Li*, Hao Li, Ming Li, Haiyang Huang and Fuwan Gan

*Address all correspondence to: waylee@mail.sim.ac.cn

State Key laboratory of Functional Materials for Informatics, Shanghai Institute of Microsystem and Information Technology, Chinese Academy of Sciences, China

References

[1] H. S. Eisenberg, Y. Silberberg, R. Morandotti, and J. S. Aitchison, "Diffraction management," Phys. Rev. Lett., Vol. 85, pp. 1863–1866, Aug. 2000.

[2] W. Chen, and D. L. Mills, "Gap solitons and the nonlinear optical response of superlattices," Phys. Rev. Lett., Vol. 58, pp. 160–163, Jan. 1987.

[3] B. J. Eggleton, R. E. Slusher, C. M. de Sterke, P. A. Krug, and J. E. Sipe, "Bragg grating solitons," Phys. Rev. Lett., Vol. 76, pp. 1627–1630, Mar. 1996.

[4] H. Kosaka, T. Kawashima, A. Tomita, M. Notomi, T. Tamamura, T. Sato, and S. Kawakami, "Self-collimating phenomena in photonic crystals," Appl. Phys. Lett., Vol. 74, no. 9, pp. 1212–1214, 1999.

[5] L. L. Zhang, Q. W. Zhan, J. Y. Zhang, and Y. P. Cui, "Diffraction inhibition in two-dimensional photonic crystals," Opt. Lett., Vol. 36, no. 5, pp. 651–653, Mar. 2011.

[6] Y. Jin, and S. He, "Canalization for subwavelength focusing by a slab of dielectric photonic crystal," Phys. Rev. B., Vol. 75, p. 195126, May. 2007.

[7] P. A. Belov, C. R. Simovski, and P. Ikonen, "Canalization of subwavelength images by electromagnetic crystals," Phys. Rev. B., Vol. 71, p. 193105, May. 2005.

[8] R. S. Chu, and T. Tamir, "Group velocity in space-time periodic media," Electron. Lett., Vol. 7, no. 14, pp. 410–412, 1971.

[9] T. Yamashita, and C. J. Summers, "Evaluation of self-collimated beams in photonic crystals for optical interconnect," IEEE J. Sel. Area. Comm., Vol. 23, no. 7, pp. 1341–1347, Jul. 2005.

[10] C. Lv, W. Li, X. Y. Jiang, and J. C. Cao, "Far-field super-resolution imaging with a planar hyperbolic metamaterial lens," Europhys. lett., Vol. 105, no. 2, Jan. 2014.

[11] H. Li, A. Wu, W. Li, X. Lin, C. Qiu, Z. Sheng, X. Wang, S. Zou, and F. Gan, "Millimeter-scale and large-angle self-collimation in a photonic crystal composed of silicon nanorods," IEEE Photonics J., Vol. 5, no. 2, pp. 2201306–2201306, Apr. 2013.

[12] P. T. Rakich, M. S. Dahlem, S. Tandon, M. Ibanescu, M. Soljacic, G. S. Petrich, J. D. Joannopoulos, L. A. Kolodziejski, and E. P. Ippen, "Achieving centimetre-scale supercollimation in a large-area two-dimensional photonic crystal," Nat. Mater., Vol. 5, pp. 93–96, Feb. 2006.

[13] T. Shih, A. Kurs, M. Dahlem, G. Petrich, M. SoljaCic, E. Ippen, L. Kolodziejski, K. Hall, and M. Kesler, "Supercollimation in photonic crystals composed of silicon rods," Appl. Phys. Lett., Vol. 93, no. 13, p. 131111, 2008.

[14] V. Mocella, S. Cabrini, A. S. P. Chang, P. Dardano, L. Moretti, I. Rendina, D. Olynick, B. Harteneck, and S. Dhuey, "Self-collimation of light over millimeter-scale distance in a quasi-zero-average-index metamaterial," Phys. Rev. Lett., Vol. 102, p. 133902, Apr. 2009.

[15] M. Qi, E. Lidorikis, P. T. Rakich, S. G. Johnson, J. Joannopoulos, E. P. Ippen, and H. I. Smith, "A three-dimensional optical photonic crystal with designed point defects," Nature, Vol. 429, no. 6991, pp. 538–542, Jun. 2004.

[16] Z. Lu, S. Shi, J. A. Murakowski, G. J. Schneider, C. A. Schuetz, and D. W. Prather, "Experimental demonstration of self-collimation inside a three-dimensional photonic crystal," Phys. Rev. Lett., Vol. 96, p. 173902, May 2006.

[17] H. Abdi, "The method of least squares," in Encyclopedia of research design. Thousand Oaks, CA, USA: Sage. pp. 705–708, 2007.

[18] H. Li, W. Li, J.-J. Du, A.-M. Wu, C. Qiu, Z. Sheng, X. Wang, S.-C. Zou, and F.-W. Gan, "Optical total reflection and transmission with mode control in a dielectric subwavelength nanorod chain," Chin. Phys. B., Vol. 22, no. 11, p. 117807, Nov. 2013.

[19] Y. Xu, X. Chen, S. Lan, Q. Guo, W. Hu, and L. Wu, "The all-angle self-collimating phenomenon in photonic crystals with rectangular symmetry," J. Opt. A: Pure Appl. Op., Vol. 10, no. 8, p. 085201, 2008.

[20] J. Witzens, M. Loncar, and A. Scherer, "Self-collimation in planar photonic crystals," IEEE J. Sel. Top. Quantum Electron., Vol. 8, no. 6, pp. 1246–1257, nov/dec. 2002.

[21] Li. Ming, Li. Wei, Haiyang Huang, Jing Wang, Li. You, Wu. Aimin, Zhen Sheng, Xi Wang, Shichang Zou, Fuwan Gan, "All-angle quasi-self-collimation effect in a rod-type silicon photonic crystal," IEEE Photonic J., Vol. 7, no. 1, p. 4700108, Feb. 2015.

[22] J. D. Joannopoulos, S. G. Johnson, J. N. Winn, and R. D. Meade, "Photonic crystals: molding the flow of light (Second Edition)," 2nd ed. Princeton University Press, Princeton, USA. Feb. 2008.

[23] A. Yariv, Y. Xu, R. K. Lee, and A. Scherer, "Coupled-resonator optical waveguide: a proposal and analysis," Opt. Lett., Vol. 24, no. 11, pp. 711–713, Jun. 1999.

[24] L. Gan, F. Qin, and Z. Li, "Broadband large-angle self-collimation in two-dimensional silicon photonic crystal," Opt. Lett., Vol. 37, no. 12, pp. 2412–2414, Jun. 2012.

[25] W. Li, Z. Liu, X. Zhang, and X. Jiang, "Switchable hyperbolic metamaterials with magnetic control," Appl. Phys. Lett., Vol. 100, no. 16, pp. 16108-1–16108-5, Apr. 2012.

[26] V. Mocella, P. Dardano, L. Moretti, and I. Rendina, "Influence of surface termination on negative reflection by photonic crystals," Opt. Exp., Vol. 15, no. 11, pp. 6605–6611, May. 2007.

[27] L. Lin and Z. Li, "Sensitivity to termination morphology of light coupling in photonic-crystal waveguides," Phys. Rev. B., Vol. 69, no. 19, pp. 193103-1–193103-4, May. 2004.

[28] Haiyang Huang, Li. Hao, Li. Wei, Wu. Aimin, Xin Chen, Xuefeng Zhu, Zhen Sheng, Shichang Zou, Xi Wang, and Fuwan Gan, "High-efficiency vertical light emission through a compact silicon nanoantenna array," ACS Photonics, Vol. 3, no. 3, pp. 324–328, Feb. 2016.